

Global Study of the Simplest Scalar Phantom Dark Matter Model

Kingman Cheung^{1,2}, Yue-Lin S. Tsai³, Po-Yan Tseng²,

Tzu-Chiang Yuan⁴ and A. Zee^{4,5}

¹*Division of Quantum Phases & Devices, School of Physics,*

Konkuk University, Seoul 143-701, Korea

²*Department of Physics, National Tsing Hua University, Hsinchu 300, Taiwan*

³*National Center for Nuclear Research, Hoza 69, 00-681 Warsaw, Poland*

⁴*Institute of Physics, Academia Sinica, Nankang, Taipei 11529, Taiwan*

⁵*Kavli Institute for Theoretical Physics,*

University of California, Santa Barbara, CA 93106

(Dated: October 9, 2018)

Abstract

We present a global study of the simplest scalar phantom dark matter model. The best fit parameters of the model are determined by simultaneously imposing (i) relic density constraint from WMAP, (ii) 225 live days data from direct experiment XENON100, (iii) upper limit of gamma-ray flux from Fermi-LAT indirect detection based on dwarf spheroidal satellite galaxies, and (iv) the Higgs boson candidate with a mass about 125 GeV and its invisible branching ratio no larger than 40% if the decay of the Higgs boson into a pair of dark matter is kinematically allowed. The allowed parameter space is then used to predict annihilation cross sections for gamma-ray lines, event rates for three processes mono- b jet, single charged lepton and two charged leptons plus missing energies at the Large Hadron Collider, as well as to evaluate the muon anomalous magnetic dipole moment for the model.

I. INTRODUCTION

Evidences for the existence of dark matter are mainly coming from cosmological observations related to the physics of gravity. These include the relic density of dark matter, anisotropies in the Cosmic Microwave Background (CMB), large scale structure of the universe, as well as the bullet clusters and the associated gravitational lensing effects. While we still do not know what the nature of dark matter is, it is clear that there is no room to accommodate dark matter in the standard model (SM) of particle physics based on gauge invariance of $SU(3)_C \times SU(2)_L \times U(1)_Y$ and Einstein-Hilbert gravity theory based on general coordinate invariance. While it is plausible that the nature of dark matter may have a purely gravitational origin, theories that have been put forward thus far are not as convincing as those from the particle physics point of view. In particular the relic density strongly suggests that dark matter may be a weakly interacting massive particle (WIMP). If dark matter can indeed be related to weak scale physics, there may be hope for us to detect them in various underground experiments of direct detection as well as in space experiments using balloons, satellites, or space station of indirect detection. Furthermore, WIMP dark matter might be produced directly at the Large Hadron Collider (LHC) by manifesting itself as missing energy with a spectrum that may be discriminated from standard model background of neutrinos.

In this paper, we will focus on the simplest dark matter model [1] which is based on adding a real singlet scalar field to the SM. The communication between the scalar dark matter and the SM gauge bosons and fermions must then go through the SM Higgs boson. While there have been many studies for this simple model and its variants in the literature [2–7], we believe a global study of this model is still missing. In this work, we will fill this gap. We use the current experimental constraints of relic density from WMAP [8], 225 live days data from direct experiment XENON100 [9], diffuse gamma-ray flux from indirect detection experiment of Fermi-LAT using the dwarf spheroidal satellite galaxies (dSphs) [10, 11], and a Higgs boson candidate with mass about 125 GeV reported recently by the LHC [12, 13] to deduce the best fit parameters of the model. The deduced parameters are used to predict various phenomenology of the model at the LHC, including production of the mono- b jet, single charged lepton, and two charged leptons plus missing energies. We also evaluate the muon anomalous magnetic dipole moment which is a two loop process in the model. For a

global fitting based on effective operators approach, see our recent work in [14]. A similar global analysis for isospin violating dark matter is presented in [15].

In the next section, we will briefly review the scalar phantom model of dark matter. In section III, we present the global fitting for the relevant parameters of the model using the various experimental constraints described above. In section IV, we discuss collider phenomenology and the muon anomalous magnetic dipole moment of the model. We conclude in section V. Some analytical formulas of the matrix elements needed in our analysis as well as the expression for the muon anomalous magnetic dipole moment are collected in the Appendix.

II. THE SCALAR PHANTOM MODEL

The simplest dark matter model (SZ) [1] (dubbed scalar phantom by the authors in [1]) is obtained by adding one real singlet scalar χ in addition to the Higgs doublet Φ to the SM. The scalar part of the Lagrangian is given by

$$\mathcal{L}_{\text{scalar}} = (D^\mu \Phi)^\dagger (D_\mu \Phi) - \lambda \left(\Phi^\dagger \Phi - \frac{\mu^2}{2\lambda} \right)^2 + \frac{1}{2} \partial^\mu \chi \partial_\mu \chi - \frac{1}{2} m^2 \chi^2 - \frac{1}{4!} \eta \chi^4 - \frac{1}{2} \rho \chi^2 \Phi^\dagger \Phi . \quad (1)$$

A discrete Z_2 symmetry of $\chi \rightarrow -\chi$ while keeping all SM fields unchanged has been imposed to eliminate the χ , $\chi \Phi^\dagger \Phi$, and χ^3 terms. As a result it guarantees the stability of the χ particle and hence it may be a viable candidate for WIMP (weakly interacting massive particle) dark matter. Note that the χ^4 term in Eq.(1) implies a contact interaction vertex among the scalar dark matter.

The virtue of this model is its simplicity. Indeed, it represents the simplest realization of a broad class of models, in which we could add any number of singlet scalar χ to the standard model, or the standard model augmented by a private Higgs sector [16]. The analysis given here is in the spirit of seeing whether or not the simplest version of this kind of model could now be ruled out.

After electroweak symmetry breaking, Φ develops a vacuum expectation value $v/\sqrt{2}$, where $v = \mu/\sqrt{\lambda} = 246$ GeV. After making the shift $\Phi(x)^T = (0, v + H(x))/\sqrt{2}$, the physical Higgs field H obtains a mass $m_H = \sqrt{2}\lambda v = \sqrt{2}\mu$ and the last term in Eq.(1) becomes

$$-\frac{1}{2} \rho \chi^2 \Phi^\dagger \Phi \longrightarrow -\frac{1}{4} \rho v^2 \chi^2 - \frac{1}{2} \rho v H \chi^2 - \frac{1}{4} \rho H^2 \chi^2 . \quad (2)$$

The first term on the right handed side of Eq.(2) implies the dark matter χ also pick up an additional contribution of $\frac{1}{2}\rho v^2$ to its mass, thus $m_\chi^2 = m^2 + \frac{1}{2}\rho v^2$. We will assume m_χ^2 is always positive so that the Z_2 symmetry will never be broken, except perhaps due to black hole effects. The second term in Eq. (2) tells us that the dark matter χ can communicate to the SM fields and self-interact with itself via a tree level Higgs exchange, while the last term contributes to the relic density calculation from the process $\chi\chi \rightarrow HH$ if kinematically allowed. If kinematics permits, the second term also allows Higgs boson to decay into a pair of χ , giving rise to the invisible Higgs width. Implication of invisible Higgs width in the Higgs search at the LHC will be discussed further in the following sections.

There are a few theoretical restrictions on the model, including vacuum stability, unitarity, and triviality. Stability of the vacuum requires the scalar potential be bounded from below. At tree level, we have

$$\lambda > 0, \eta > 0, \rho^2 < \frac{2\lambda\eta}{3}. \quad (3)$$

Tree level perturbative unitarity constraints can be deduced by considering the longitudinal gauge boson scatterings [17] as well as all scalar-scalar scatterings [5]

$$m_H^2 < \frac{8\pi}{3}v^2 \approx (712 \text{ GeV})^2, \quad \eta < 8\pi, \quad \text{and} \quad |\rho| < 8\pi. \quad (4)$$

Analysis of the triviality of this model can be found in the literature [5, 6].

Self-interacting cold dark matter was proposed in [18] to resolve some conflicts between actual observations and WIMP theory which predicts overly dense cores in the center of galaxies and clusters and an overly large number of halos within the Local Group. The Spergel-Steinhardt bound [18] for collisional (self-interacting) dark matter,

$$2 \times 10^3 \text{ GeV}^{-3} \leq \frac{\sigma_{\chi\chi \rightarrow \chi\chi}}{m_\chi} \leq 3 \times 10^4 \text{ GeV}^{-3}, \quad (5)$$

can be used to constrain the contact self-coupling η of the scalar phantom (as well as the coupling ρ through Higgs exchange). We refer to previous works [3, 19] on this issue.

III. GLOBAL FITTING

In this section, we consider the global constraints coming from WMAP relic density [8], the XENON100 data [9], the Fermi-LAT upper limit of diffuse gamma-ray flux based on dSphs [10], the LHC Higgs mass around 125 GeV [12, 13], and the upper limit of Higgs

invisible decay branching ratio [20]. The relevant parameters of the model are the dark matter mass m_χ , the coupling ρ and the Higgs mass m_H , which the likelihood functions will depend on. The publicly available software package MicrOMEGAs version 2.4.5 [21] is used to calculate the relic density and gamma-ray flux.

A. WMAP Relic Density

In the calculation of the relic density, we consider all of the following two body tree level processes

$$\chi\chi \rightarrow H^{(*)} \rightarrow f\bar{f}, W^+W^-, ZZ, HH . \quad (6)$$

The relic density from the WMAP 7-year result [8] is

$$\Omega_c h^2 = 0.112 \pm 0.0056 , \quad (7)$$

where Ω_c is the density of the cold dark matter normalized to the critical density and h is the Hubble rate in unit of $100 \text{ km sec}^{-1} \text{ Mpc}^{-1}$. In the fitting, we use the Gaussian distribution for the WMAP relic density in our likelihood function,

$$\mathcal{L}_{\text{relic}} = e^{-\frac{\chi^2}{2}} , \quad (8)$$

with the χ^2 defined as ¹

$$\chi^2 = \frac{(\text{prediction} - \text{experimental central value})^2}{\sigma^2 + \tau^2} , \quad (9)$$

where the σ can be read off from the WMAP experimental error [8]. We also assume a theoretical uncertainty τ to be 10% of the prediction in order to account for the discrepancy due to different methods being used to solve the Boltzmann equation in different relic density computation packages.

Our working assumption is that the WMAP data on relic density constrains the current model without affecting other cosmological parameters in a significant way.

¹ We apologize for abusing our notation of χ to stand for the scalar phantom dark matter as well as to define the chi-squared.

B. Direct Detection

Here we need to calculate the elastic cross section for

$$\chi\mathcal{N} \longrightarrow \chi\mathcal{N}, \quad (10)$$

where \mathcal{N} is a nucleus with Z protons and $(A - Z)$ neutrons. For a Higgs mass around 125 GeV, it is heavy enough to be integrated out to give an effective local interaction between the dark matter and the quarks. Since the local velocity of the dark matter is about $v_\chi \sim 10^{-3}c$, non-relativistic reduction is appropriate. For the present model there is no spin-dependent cross section for the above elastic scattering, because the dark matter is a scalar particle. The spin-independent cross section at zero recoil energy can be obtained as

$$\sigma_{\chi\mathcal{N}}^{\text{SI}}(0) = \frac{1}{4\pi} \mu_{\chi\mathcal{N}}^2 |Zf_p + (A - Z)f_n|^2, \quad (11)$$

where $\mu_{\chi\mathcal{N}} = m_\chi m_{\mathcal{N}} / (m_\chi + m_{\mathcal{N}})$ is the reduced mass for the $\chi\mathcal{N}$ system and

$$f_N = \rho \frac{m_N}{m_\chi m_H^2} \left\{ \sum_{q=u,d,s} f_{Tq}^{(N)} + \frac{2}{27} n_Q f_{TG}^{(N)} \right\} \quad (12)$$

with n_Q denotes the number of heavy quarks and $N = p$ or n . The factors $f_{Tq}^{(N)}$ and $f_{TG}^{(N)}$ are hadronic matrix elements, and we will use their default values given in MicrOMEGAs [21].

For direct detection we choose the truncated Maxwell velocity distribution, which is the default choice in MicrOMEGAs. Because XENON100 is a counting experiment, the best choice for the likelihood function is Poisson distribution,

$$\mathcal{L}_{\text{direct}} \propto \frac{e^{-(s+b)} (s+b)^o}{o!}. \quad (13)$$

The $b = 1.0$ and $o = 2.0$ are the number of background and observation events taken from XENON100 [9], respectively. In order to achieve the minimum of χ_{direct}^2 equals to zero, we normalized Eq. (13) by the factor $e^{-o} (o)^o / o!$. For simplicity we do not take the background uncertainties into account in our analysis. The signal s equals $\varepsilon \times N(\text{unbiased})$ in the nuclear recoil energy range of 6.6 - 30.5 keV_{nr}, where ε is the detector efficiency once the experimental cuts are applied to the total number of unbiased events $N(\text{unbiased})$. In other words, ε is the fraction of $N(\text{unbiased})$ generated by the Monte-Carlo simulation which survives the various cuts taken in XENON100.

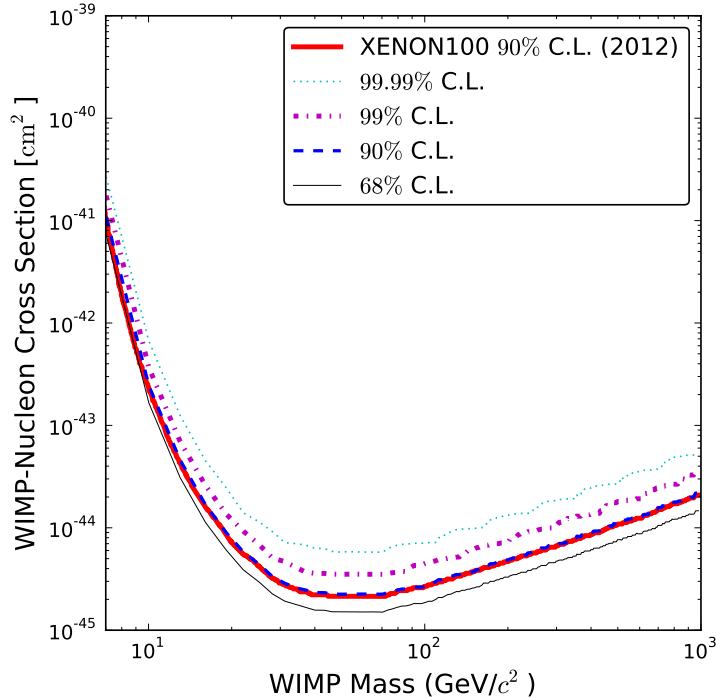


FIG. 1. Our approximation of the XENON100 likelihood map as described in the text. The dashed blue line shows the 90.0% CL bound. It approximately equals to the XENON100 90% CL exclusion contour, shown by the thick solid red line. The thin solid black line, the dashed magenta line, and the cyan dotted line show our calculations of the 68.0% CL, the 99.0% CL, and 99.99% exclusion bound, respectively.

We use the following approximate method to evaluate the efficiency ε as a function of m_χ . First, from XENON100 data of $b = 1.0$ and $o = 2.0$ at 90% C.L. one can obtain a reference $s^* = 5.72$ using the likelihood function just mentioned. Then, taking the values of m_χ and $\sigma_{\chi p}^{\text{SI}}$ along the 90% C.L. line from Fig. 3 in [9] as input to MicrOMEGAs, we can obtain $N(\text{unbiased})$ which is a function of m_χ and $\sigma_{\chi p}^{\text{SI}}$. Hence, assuming the efficiency ε depends only on m_χ and $\sigma_{\chi p}^{\text{SI}}$, it is simply given by the ratio $s^*/N(\text{unbiased})$. Below when we compute the number of events for our model, we will multiply it by this ε to obtain the corresponding number of signals. For Poisson distribution we evaluate the effective χ^2 according to the following expression

$$\chi^2 = -2 \ln \mathcal{L} . \quad (14)$$

In order to justify our simple treatment of the likelihood function shown in Eq. (13), we

plot the 68%, 90%, 99%, and 99.99% C.L. curves, and compare to the published XENON100 90% C.L. curve in Fig. (1). It is clear that our 90% C.L. curve is almost identical to the one from XENON100. Therefore, we can safely use the likelihood function in Eq. (13).

C. Indirect Detection

Since the couplings of the scalar dark matter to the SM fermions must go through the Higgs exchange in the SZ model, the positron flux and the anti-proton flux are probably too small for indirect detection ². We will focus on gamma-ray flux in indirect detection ³. For continuum gamma-ray, the relevant processes in the model are $f\bar{f}$, W^+W^- , ZZ , and HH channels. The W^+W^- , ZZ , and HH will subsequently decay into quarks and charged leptons which can produce gamma-rays. However, the HH final state will be discarded in our later numerical analysis since micrOMEGAs does not provide the Pythia decay table of $\chi\chi \rightarrow HH \rightarrow \dots \rightarrow$ gamma-rays. Furthermore, Fermi-LAT [10] has neither the limit for HH nor ZZ final state. Nevertheless, the HH contribution to gamma rays is expected to be small, since the Higgs decays into SM fermion pairs are suppressed by the fermion mass. When $m_\chi > m_W$, the dominant contribution comes from W^+W^- , and the next largest contribution comes from the heaviest fermion pair that the $\chi\chi$ can annihilate into. For lower DM mass, the dominant process is the following annihilation

$$\chi\chi \rightarrow H^{(*)} \rightarrow q\bar{q} \rightarrow \pi^0 X \rightarrow 2\gamma X \quad (15)$$

where the neutral pion coming from quark fragmentation decays into two photons.

Detection of one or more spectral lines would be the smoking gun signal for dark matter. The following annihilation processes $\chi\chi \rightarrow \gamma\gamma$, γZ , γH can give rise to discrete gamma lines. In the SZ model, only the following two processes

$$\chi\chi \rightarrow H^{(*)} \rightarrow \gamma\gamma, \gamma Z \quad (16)$$

are possible ⁴. The γZ final state is possible if $m_\chi > m_Z/2$. The gamma-ray lines are located approximately at energies $E_\gamma \sim m_\chi$ and $m_\chi(1 - m_Z^2/4m_\chi^2)$ for the two final states

² However, it was shown in [22] that antimatter signals for the present model might be promising at the AMS experiment on the space station.

³ An earlier analysis of the gamma-ray signals for the present model can be found in [23].

⁴ By charge conjugation, it is impossible to construct gauge invariance operators using one single photon field strength with arbitrary numbers of Higgs fields and partial derivatives.

$\gamma\gamma$ and γZ , respectively, with corrections of order $(v_\chi/c)^2 \sim 10^{-6}$, which is minuscule. Since these processes are one-loop induced and therefore suppressed, we do not include them in the global fitting. Instead, we will compute these cross sections after the scan and compare with the Fermi-LAT limits [24].

The dSphs of our Milky Way are satellite systems without active star formation or detected gas content. They are thus fainter and expected to be dominated by DM due to their own gravitational binding. Although the expected flux of gamma-rays is not as high as the Galactic Center, these dwarf galaxies may have a better signal-to-noise ratio. Currently, the most stringent upper limits on the DM annihilation cross sections in various channels are derived by Fermi-LAT Collaboration using the new 24 months data set with the following two improvements on their analysis [10]. First, they performed a joint likelihood analysis to 10 satellite galaxies which can improve their statistical power. Second, they included the uncertainties in the dark matter distribution in these satellites entered in the astrophysical J factor

$$J(\psi) = \int_{\text{line-of-sight}, \Delta\Omega} dl d\Omega \rho^2[l(\psi)] , \quad (17)$$

which is the line-of-sight integral of the squared DM density, ρ , toward an observational direction, ψ , integrated over a sustained solid angle, $\Delta\Omega$. The gamma-rays flux is then given by

$$\phi(E, \psi) = \frac{1}{8\pi m_\chi^2} \langle \sigma v_\chi \rangle N_\gamma(E) J(\psi) , \quad (18)$$

where $\langle \sigma v_\chi \rangle$ is the velocity-averaged pair annihilation cross section and $N_\gamma(E)$ is the gamma-ray energy distribution per annihilation. Based on these two improvements, robust upper limits of 95% C.L. on the σv_χ for the $b\bar{b}$, $\tau^+\tau^-$, $\mu^+\mu^-$, and W^+W^- channels are derived in [10]. We will use these constraints on the diffuse gamma-ray flux in our global fitting. Since each limit was obtained by assuming the dominance by one single channel, we can approximately reconstruct the upper limit suitable to our case by applying the same method as in Sec. 4.1 of [25].

In our analysis for dSphs, we adopt our likelihood function as follows

$$\mathcal{L}_{\text{indirect}} = \text{erfc} \left(\frac{\sigma v_\chi - \sigma v_{\chi 95}}{\sqrt{2}\tau} \right) / \text{erfc} \left(\frac{-\sigma v_{\chi 95}}{\sqrt{2}\tau} \right) , \quad (19)$$

where $\text{erfc} = 1 - \text{erf}$ is the complementary error function and the effective χ^2 is the same as Eq.(14). In addition, because the astrophysical J factor is expected to have a 3% uncertainty and the hadronization/decay tables in either MicrOMEGAs [21] or DarkSUSY

[26] have a factor of 2 uncertainty, we can then include the theoretical uncertainties as $\tau = \sqrt{0.03^2 + 2^2} \times \sigma v_{\chi 95}$, where $\sigma v_{\chi 95}$ is the 95% C.L. of the reconstructed upper limit for our DM pair annihilation cross section.

D. Higgs Mass and Its Invisible Width

In order to force our scan to go to the $m_H \sim 125$ GeV region, as suggested by the recent LHC data [12, 13], we use the Gaussian likelihood function for the Higgs mass with a central value of 125.3 GeV and an experimental uncertainty $\sigma \sim 0.6$ GeV. Since the m_H is an input, we do not introduce any theoretical error for the Higgs mass. Therefore, the likelihood function for the Higgs mass is

$$\mathcal{L}_{\text{Higgs}} = e^{-\frac{1}{2} \frac{(m_H - 125.3 \text{ GeV})^2}{\sigma^2}}. \quad (20)$$

It has been pointed out recently in [20] that the monojet search at the LHC has strongly disfavored $B_{\text{inv}} \equiv \Gamma_{\text{inv}} / (\Gamma_{\text{SM}} + \Gamma_{\text{inv}}) > 0.4$ for Higgs-portal dark matter model where Γ_{SM} is the total SM Higgs width. The invisible width of SM Higgs in the SZ model is

$$\Gamma_{\text{inv}}(H \rightarrow \chi\chi) = \frac{1}{32\pi} \frac{\rho^2 v^2}{m_H} \left(1 - \frac{4m_\chi^2}{m_H^2}\right)^{\frac{1}{2}}. \quad (21)$$

We note that the invisible decay mode is not dominant in most of dark matter mass range. Only when $m_H < 130$ GeV and $m_H > 2m_\chi$, the invisible decay of Higgs becomes significant. Hence, we implement the Higgs invisible decay as a 0/1 hard cut. If $m_H < 130$ GeV, $m_H > 2m_\chi$, and $B_{\text{inv}}(H \rightarrow \chi\chi) > 0.4$, we multiply $\mathcal{L}_{\text{Higgs}}$ by 0, otherwise by 1.

E. Parameter Scan

Engaging with MultiNest v2.7 [27] with 10000 living points, a stop tolerance factor 0.001, and an enlargement factor reduction parameter 0.5, we perform a random scan in the three dimensional parameter space of m_χ , ρ , and m_H restricted in the following ranges

$$\begin{aligned} 1.0 &\leq \log_{10}[m_\chi / \text{GeV}] \leq 3.0 \\ -3.0 &\leq \log_{10}[\rho] \leq 0.0 \\ 114.0 \text{ GeV} &\leq m_H \leq 130.0 \text{ GeV} \end{aligned} \quad (22)$$

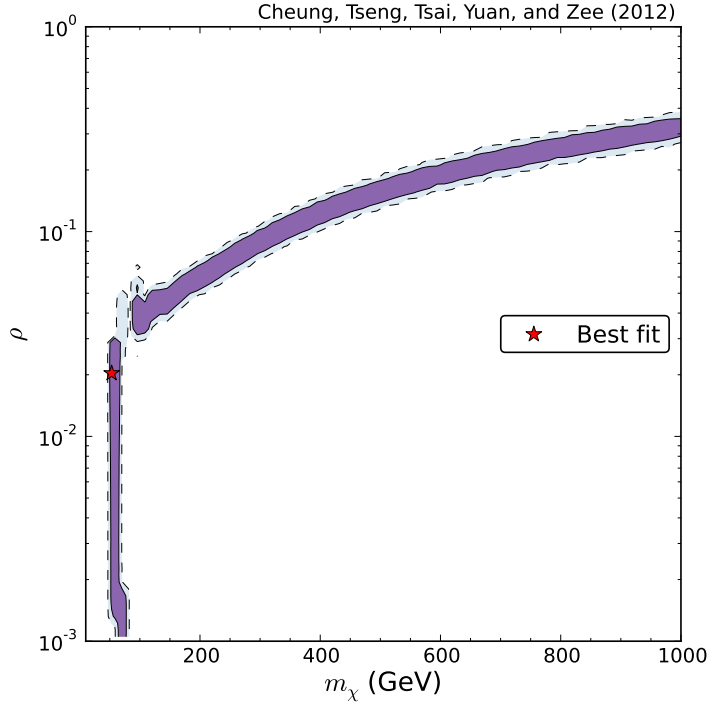


FIG. 2. The profile likelihood of (m_χ, ρ) for the SZ model by the global fitting using WMAP relic density [8], XENON100 [9], dSphs [10] and a 125 GeV Higgs [12, 13] with an invisible branching ratio less than 40%.

The selected scan range of ρ is much smaller than the theoretical limit $|\rho| < 8\pi$ because the WMAP window is very small which only allows $\rho < 1$. Furthermore, in order to scan efficiently in the Higgs resonance region and cover the low ρ region, we use the log priors for m_χ and ρ as specified in Eq.(22). Similar results are found for the case of negative ρ and will not be shown here.

After hitting the stop criteria, we collect total 440682 samples, and plot 68% and 95% profile likelihood confidence limit contours based on 138017 samples which are selected by Nested Sampling algorithm [28]. The 68% and 95% confidence limit means that the total likelihood is greater than $0.32 * \mathcal{L}(\text{Best Fit})$ and $0.05 * \mathcal{L}(\text{Best Fit})$, respectively.

The total likelihood function for our global fitting will be taken as

$$\mathcal{L}_{\text{tot}} = \mathcal{L}_{\text{relic}} \times \mathcal{L}_{\text{direct}} \times \mathcal{L}_{\text{indirect}} \times \mathcal{L}_{\text{Higgs}} , \quad (23)$$

and the effective total χ_{tot}^2 is given by

$$\chi_{\text{tot}}^2 = -2 \ln \mathcal{L}_{\text{tot}} . \quad (24)$$

Our analysis uses the method of maximum likelihood. The likelihood function of each experiment is listed clearly in Eq. (8) for relic density, in Eq. (13) for the XENON100 data, in Eq. (19) for the gamma-ray data of Fermi-LAT, and in Eq.(20) that for the Higgs boson mass. The joint likelihood is then the product of all these likelihood functions, as given in Eq. (23). The “best fit” point in Fig. 2 presented below (as well as in Fig. 3) is the point in the parameter space such that the joint likelihood function is maximum there. The 1σ and 2σ regions in these figures are the 1σ and 2σ deviations relative from the “best fit” point.

The result of the profile likelihood projected on the (m_χ, ρ) plane is shown in Fig. (2). We can clearly see that there are two branches: the vertical branch at low m_χ region and the horizontal branch hooked around at $m_\chi > 100$ GeV. The shape of these two branches is mainly due to the relic density constraint. However, XENON100 and dSphs also play a significant role at the junction of the two branches, $\rho \approx 0.04 - 0.1$ and $50 < m_\chi/\text{GeV} < 200$, where relatively large $\sigma_{\chi p}^{\text{SI}}$ and σv can be easily produced. Furthermore, the hard cut due to the Higgs invisible branching ratio can remove some of the parameter space points with $50 < m_\chi/\text{GeV} < 100$ and $0.03 < \rho < 0.1$. On the other hand, it is hard to satisfy our constraints in the region $m_\chi < 50$ GeV, because the χ^2 in this region rises sharply due to the Higgs boson mass and relic density constraints. The vertical branch in the figure is mainly due to the Higgs resonance effect, which can efficiently enhance the dark matter annihilation cross section when $2m_\chi$ falls near m_H . Hence, the coupling ρ has to be small correspondingly, in order to be consistent with WMAP data. On the other hand, when $m_\chi > m_W$, the $\chi\chi \rightarrow W^+W^-$ channel dominates the annihilation cross section [2, 3, 29]. Therefore, we can see from the figure that in the 1 and 2 σ C.L. bands of the horizontal branch the allowed ρ is roughly proportional to m_χ^2 (see Eq.(34) at the Appendix).

In Fig. 3, we show the profile likelihood on $m_\chi - \sigma_{\chi p}^{\text{SI}}(0)$ panel against the experimental 90% C.L. upper limit from XENON100. Clearly, the XENON100 data is only able to rule out $50 \text{ GeV} \lesssim m_\chi \lesssim 100 \text{ GeV}$. Current DM direct detection cannot constrain most of the parameters. On the other hand, the Higgs resonance region and most of the horizontal band can be tested in the future by XENON-1T (see the dashed line in Fig. 3).

Other than the Higgs resonance region, the WMAP constraint dominates the likelihood function as shown in Fig. (3), and therefore the largest likelihood of XENON100 only occurs at $s \ll b$. Nevertheless, it is easier to satisfy the relic density constraint in the Higgs resonance region, and therefore the largest likelihood of XENON100 in the Higgs resonance

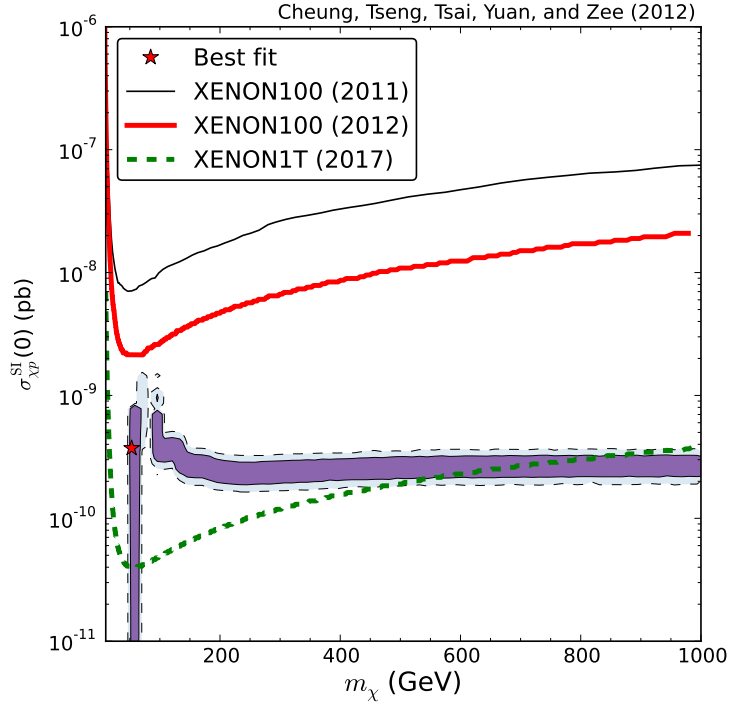


FIG. 3. The profile likelihood of the spin-independent cross section $\sigma_{\chi p}^{\text{SI}}(0)$ for the SZ model projected onto the m_{χ} axis. The latest XENON100 limits [9] are overlaid for comparison. The projected XENON-1T sensitivity is also shown.

region occurs at $s = 1.0$ such that $s+b = o$, by fine-tuning m_{χ} , ρ , and m_H . As a consequence, the best fit of our scan appears in the Higgs resonance region.

IV. PHENOMENOLOGY

With the result of the likelihood determined, we can proceed to evaluate other observables as predictions for the model, including gamma-ray lines, collider signatures, and muon anomalous magnetic dipole moment.

A. Gamma-Ray Lines

In Fig.(4), we plot the cross sections for the gamma-ray line in the SZ model versus the profile likelihood projected onto the m_{χ} axis. The left panel is for $\chi\chi \rightarrow \gamma\gamma$ while the right one is for $\chi\chi \rightarrow \gamma Z$. The Fermi-LAT data [24] associated with different halo profiles are also

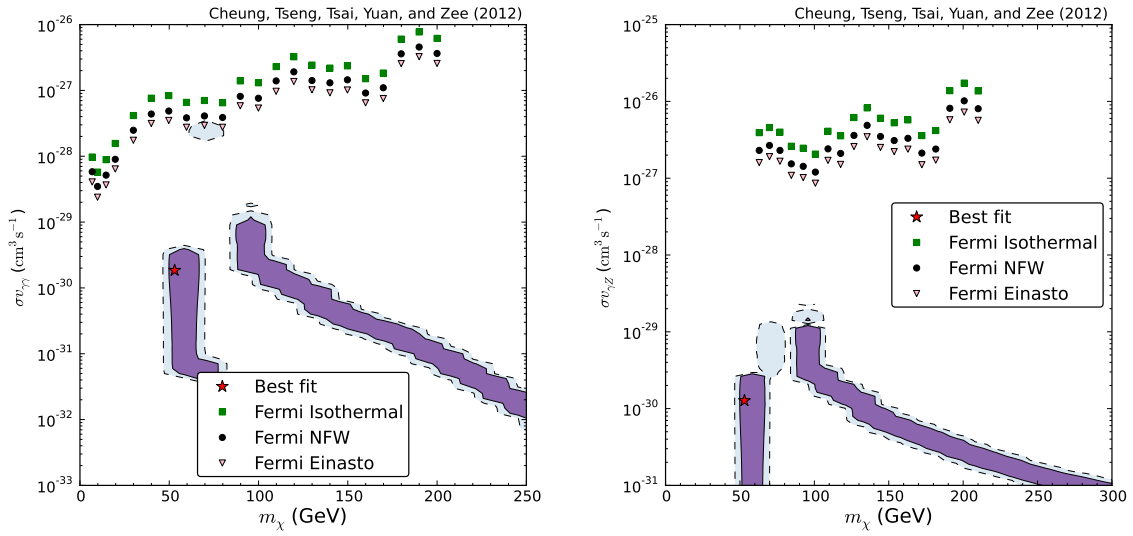


FIG. 4. The annihilation cross sections for the gamma-ray line from $\chi\chi \rightarrow \gamma\gamma$ (left) and $\chi\chi \rightarrow \gamma Z$ (right).

shown for comparisons. It is clear to see that the prediction for the $\chi\chi \rightarrow \gamma\gamma$ annihilation cross section allowed by the profile likelihood is well below the Fermi-LAT data while that of $\chi\chi \rightarrow \gamma Z$ is even further below the Fermi-LAT data. Hopefully, future better measurements made by Fermi-LAT can put a dent in the allowed profile likelihood.

B. Collider Signatures

If the invisible mode of $H \rightarrow \chi\chi$ opens up, we should study its impact on Higgs search at the LHC; in particular its effect on the branching ratios of $H \rightarrow \gamma\gamma$, $H \rightarrow WW^*$ and ZZ^* , which apparently show some excesses over the background. Since the current CMS and ATLAS data [12, 13] showed that the excesses seen in $\gamma\gamma$, WW^* , and ZZ^* channels are consistent with the expectation of the SM Higgs boson of 125 GeV,⁵ we cannot allow the invisible decay mode to be too large; otherwise the visible mode would become inconsistent with the current data.

It is easy to show that the branching ratio for a visible mode would be its SM branching ratio multiplied by $(1 - B_{\text{inv}})$ where B_{inv} is the invisible branching ratio defined earlier as

⁵ The WW^* and ZZ^* decay modes are slightly below while the $\gamma\gamma$ mode is somewhat higher than the SM predictions.

$\Gamma_{\text{inv}}/(\Gamma_{\text{SM}}+\Gamma_{\text{inv}})$. In our scan in the previous section, we had required the invisible branching ratio $B_{\text{inv}} < 0.4$ such that each visible mode is reduced by an amount less than 40% so as not to upset the current data. If the dark matter mass $m_\chi > m_H/2$, the Higgs boson simply behaves like the SM Higgs boson.

From our scan result in Fig. 2, a few typical points which have the likelihood within 68% C.L. ($1\text{-}\sigma$ band) can be identified as follows:

1. Point A: $m_\chi = 53$ GeV, $\rho = 0.02$, $m_H = 125.3$ GeV. The invisible branching ratio is right at 0.4. The significance of this point is that the Higgs boson still has a large branching ratio into $\chi\chi$. The collider signature that we will discuss below consists of a large missing energy. This is the point with the maximum likelihood, shown by the star in Fig. 2.
2. Point B: $m_\chi = 84.0$ GeV, $\rho = 0.042$, $m_H = 125.2$ GeV. This point gives χ a mass close to m_W and hence above the Higgs decay threshold. This is the point at the low end of the second branch.
3. Point C: $m_\chi = 608.3$ GeV, $\rho = 0.189$, $m_H = 125.3$ GeV. This point gives a heavy χ that is still consistent with direct detection limits.

The most common search modes so far for the dark matter are the monojet and monophoton plus missing energies. In this model, monojet or monophoton production must go through the Higgs boson H , so that the only sizable production cross sections have to go via

$$b\bar{b} \rightarrow H \rightarrow \chi\chi, \quad gg \rightarrow \chi\chi,$$

in which we can attach a gluon to the b or g leg, or attach a photon line to the b leg. Since the b -parton luminosity is small and gluon-fusion is a loop process, the monojet or monophoton rate would be relatively small.

Since the DM candidate χ only couples to the SM particles via the Higgs boson, the χ will preferably couple to the heaviest fermion. At hadronic colliders, one of the interesting processes is

$$gb \rightarrow bH^{(*)} \rightarrow b\chi\chi, \quad (25)$$

where the superscript $(*)$ on the Higgs boson denotes that the Higgs boson could be on- or off-shell depending on the mass of χ . Obviously, it is dominated by on-shell Higgs boson for

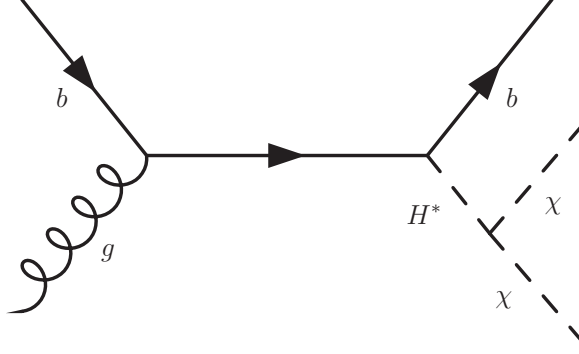


FIG. 5. A Feynman diagram showing mono- b jet production with missing energies.

$m_H > 2m_\chi$. If $m_H > 2m_\chi$ and m_H is lighter than $2m_W$, the Higgs boson will dominantly decay into a pair of χ . The corresponding collider signature would be a mono- b jet plus missing energies. The other possible signatures would be the associated production of the Higgs boson with a gauge boson W or Z :

$$pp \rightarrow W (Z) H^{(*)} \rightarrow \ell\nu (\ell^+\ell^-)\chi\chi. \quad (26)$$

The final state in this case would consist of a charged lepton or a pair of charged leptons plus missing energies.

We calculate the event rates of mono- b jet, single charged lepton, and a pair of charged leptons plus missing energies at the LHC-7, LHC-8, and LHC-14. We impose the following selection cuts for the b jet or charged leptons and the transverse missing energy

$$p_{T_b} > 30 \text{ GeV}, \quad |\eta_b| < 2; \quad p_{T_\ell} > 25 \text{ GeV}, \quad |y_\ell| < 2; \quad \cancel{p}_T > 50 \text{ GeV}. \quad (27)$$

The cross sections for the mono- b jet, single or a pair of charged lepton plus missing energies are tabulated in Table I. The largest cross section comes from mono- b jet production. However, when we apply the $\cancel{p}_T > 50$ GeV cut the cross section mono- b goes down 50 times. After further imposing the B -tagging, the event rate would only be handful. Another interesting signature is the single charged lepton plus missing energies. Counting both negatively- and positively-charged leptons the cross section could be as high as 16 fb at the LHC-8. Given the LHC-8 can accumulate 20 fb^{-1} each experiment, it would be more than 300 events each experiment. The ZH production would give, on the other hand, two charged lepton plus missing energies with a few times smaller event rates.

Note that for other typical points of the model, e.g., points B and C, the invisible decay mode of the Higgs boson is closed, and therefore the decay is similar to the SM Higgs boson.

TABLE I. Cross sections for mono- b jet, single charged lepton or a pair of charged leptons plus missing energies arise from Higgs boson production followed by $H \rightarrow \chi\chi$. We used the point A ($m_\chi = 53$ GeV, $\rho = 0.02$, and $m_H = 125.3$ GeV, $B_{\text{inv}}(H \rightarrow \chi\chi) = 0.4$). The selection cuts are defined in Eq. (27).

Subprocess	Cross sections (fb)		
	LHC-7	LHC-8	LHC-14
$gb \rightarrow bH \rightarrow b\chi\chi$	4.6	6.3	10.4
$u\bar{d} \rightarrow W^+H \rightarrow \ell^+\nu\chi\chi$	9.2	10	19
$d\bar{u} \rightarrow W^-H \rightarrow \ell^-\bar{\nu}\chi\chi$	4.7	5.8	12
$q\bar{q} \rightarrow ZH \rightarrow \ell^+\ell^-\chi\chi$	2.2	2.6	4.9

The process in Eq. (25) will then give rise to $3b$ or bWW^* final states, depending on the Higgs boson mass. The processes in Eq. (26) will give one or two charged leptons plus either $b\bar{b}$ or WW^* .

The SM background for the mono- b jet plus missing energy would be similar to the current monojet search in ATLAS [30] and CMS [31], but now with a B -tag on the monojet. The largest background [30, 31] comes from $Z + j \rightarrow \nu\bar{\nu} + j$ and $W + j \rightarrow \ell\nu + j$ with minor contributions from $t\bar{t}$, single top production, and QCD multijets when leptons or extra jets get missing down the beam. On the other hand, background events with single or double charged leptons plus large missing energy comes from $WZ \rightarrow \ell\nu\nu\bar{\nu}$ or $ZZ \rightarrow \ell\nu\bar{\nu}$ with minor contributions from $t\bar{t}$ and single top production. Precise estimations of these backgrounds are beyond the scope of the present paper.

C. Muon Anomalous Magnetic Dipole Moment

The experimental value of the muon anomalous moment $a_\mu \equiv (g_\mu - 2)/2$ is

$$a_\mu^{\text{exp}} = 116\,592\,089(63) \times 10^{-11}, \quad (28)$$

while the SM prediction is

$$a_\mu^{\text{SM}} = 116\,591\,802(49) \times 10^{-11}. \quad (29)$$

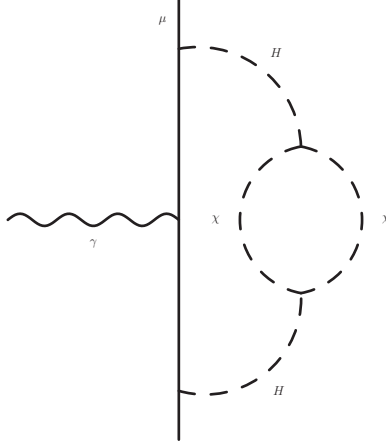


FIG. 6. Two loop Feynman diagram contributing to the muon anomalous magnetic dipole moment.

The 3.6σ discrepancy between the above experimental measurement and theoretical calculations based on using the e^+e^- annihilation cross section for the estimation of the hadronic correction [32]

$$\Delta a_\mu \equiv a_\mu^{\text{exp}} - a_\mu^{\text{SM}} = 287(80) \times 10^{-11} \quad (30)$$

could be a harbinger of various new physics beyond the SM. The contribution to the muon anomalous magnetic dipole moment a_μ in the SZ model first shows up at the two loop level (See Fig. [6]). Detailed expressions can be found in the Appendix. In Table (II), we show the numerical results of a_μ for the three typical points A, B and C from our scan. For all

TABLE II. Muon anomalous magnetic dipole moment for Points A, B and C of the likelihood.

Muon Anomalous Magnetic Dipole Moment (a_μ)		
Point A	Point B	Point C
-1.47×10^{-21}	-3.19×10^{-21}	-1.67×10^{-21}

the relevant parameter space, we have checked that the contribution is negative and many orders of magnitude below the current experimental sensitivity.

V. CONCLUSIONS

The simplest dark matter model is realized by adding a real scalar singlet to the standard model as was discussed quite some time ago in [1], long before the popular dark matter

candidate of neutralino in MSSM model took the central stage. In this work, we use the most current experimental constraints of the relic density from the 7 year WMAP data, latest XENON100 data, annihilation cross sections from Fermi-LAT based on 10 dwarf spheroidal satellite galaxies of the Milky Way, as well as the 125 GeV standard model Higgs candidate as discovered recently by the LHC, to pin down the profile likelihood for the parameters ρ and m_χ of the model.

The collected points are then used to evaluate the cross sections for the gamma-ray lines from $\chi\chi \rightarrow \gamma\gamma$ and γZ and found that they are well under the current limits from Fermi-LAT data. A small part of the allowed parameter space around $m_\chi \approx 70$ GeV barely touches the Fermi-LAT data with the Einasto halo profile. Recently, an interesting analysis in Ref.[33] using the Fermi-LAT data suggests there could be a gamma-ray line around 130 GeV that may be related to dark matter annihilation. However, other authors [34] suggest that astrophysical sources like the fermi-bubbles [35] could also be responsible for this line signal. The gamma-ray lines in this simplest dark matter model cannot accommodate this line signal based on the profile likelihood determined by the global fitting with the experimental constraints mentioned above.

We also study the LHC signals of mono- b jet, single charged lepton or a pair of charged leptons plus missing energies of the model. The most interesting case is the single charged lepton plus missing energies which can arise from associated production of WH followed by $W \rightarrow l\nu$ and invisible decay of the Higgs. With a luminosity of 20 fb^{-1} for each experiment of ATLAS and CMS at LHC-8, we expect several hundreds of such events based on the Point A.

We also evaluate the muon anomalous magnetic dipole moment of the model and found that it is many orders of magnitude below the current experimental limit for all relevant parameter space.

More stringent constraints are expected for this simple model of dark matter as more data from the LHC, direct and indirect detection experiments become available in the near future.

APPENDIX

1. Matrix Elements

In this Appendix, we list the matrix elements and annihilation cross sections for all the two body processes needed in the calculations of the relic density and indirect detection. Let s to be the center of mass energy given by $s = 4m_\chi^2/(1 - v_\chi^2/4)$ where $v_\chi = 2\beta_\chi$ with β_χ being the velocity of the dark matter. N_C is the color factor, 1 for leptons and 3 for quarks.

(1) $\chi\chi \rightarrow f\bar{f}$:

$$\sum_{\text{spin}} |\mathcal{M}|^2 = 2N_C^f \rho^2 m_f^2 \frac{s}{(s - m_H^2)^2 + m_H^2 \Gamma_H^2} \left(1 - \frac{4m_f^2}{s}\right) \quad (31)$$

$$\sigma v_\chi = \frac{1}{8\pi} N_C^f \rho^2 m_f^2 \left(1 - \frac{4m_f^2}{s}\right)^{\frac{3}{2}} \left((s - m_H^2)^2 + m_H^2 \Gamma_H^2\right)^{-1} \quad (32)$$

(2) $\chi\chi \rightarrow VV$ ($V = W$ or Z):

$$\sum_{\text{spin}} |\mathcal{M}|^2 = \rho^2 \frac{s^2}{(s - m_H^2)^2 + m_H^2 \Gamma_H^2} \left[1 - 4\left(\frac{m_V^2}{s}\right) + 12\left(\frac{m_V^2}{s}\right)^2\right] \quad (33)$$

$$\sigma v_\chi = \frac{1}{1 + \delta_{VZ}} \frac{1}{16\pi} \left(1 - \frac{4m_V^2}{s}\right)^{\frac{1}{2}} \rho^2 \frac{s}{(s - m_H^2)^2 + m_H^2 \Gamma_H^2} \left[1 - 4\left(\frac{m_V^2}{s}\right) + 12\left(\frac{m_V^2}{s}\right)^2\right] \quad (34)$$

Here δ_{VZ} is a Kronecker delta to account for the Bose statistics of the ZZ final state. We note that MicrOMEGAs computes process cross sections by CalcHEP [36]. However, we found that the amplitude squared of $\chi\chi \rightarrow W^+W^-/ZZ$ differs between Eq. (33) and the result from CalcHEP. The factor inside the square bracket of Eq. (33) is $\left[1 - 4\left(\frac{m_V^2}{s}\right) + 12\left(\frac{m_V^2}{s}\right)^2\right]$, while the corresponding factor in CalcHEP reads $\left[\frac{m_h^4}{s^2} - 4\left(\frac{m_V^2}{s}\right) + 12\left(\frac{m_V^2}{s}\right)^2\right]$. Due to this discrepancy we rescale the cross section by the ratio of these two factors.

(3) $\chi\chi \rightarrow HH$

$$\sum_{\text{spin}} |\mathcal{M}|^2 = \rho^2 \left|1 - \frac{3m_H^2}{(s - m_H^2) + im_H \Gamma_H} - \frac{\rho v^2}{t - m_\chi^2} - \frac{\rho v^2}{u - m_\chi^2}\right|^2 \quad (35)$$

$$\sigma v_\chi = \frac{1}{64\pi s} \left(1 - \frac{4m_H^2}{s}\right)^{\frac{1}{2}} \int_{-1}^1 d\cos\theta \sum_{\text{spin}} |\mathcal{M}|^2 \quad (36)$$

(4) $\chi\chi \rightarrow \gamma Z$

$$\sum_{\text{spin}} |\mathcal{M}|^2 = \frac{\rho^2 v^2}{2} \frac{(s - m_Z^2)^2}{(s - m_H^2)^2 + m_H^2 \Gamma_H^2} |\mathcal{A}_{\gamma Z}(s)|^2 \quad (37)$$

$$\mathcal{A}_{\gamma Z}(s) = \frac{eg^2}{16\pi^2 m_W} \left(-4 \cos \theta_W I'_W + \sum_f \frac{-2Q_f (T_f^{3L} - 2Q_f \sin^2 \theta_W)}{\cos \theta_W} N_C^f I'_f \right) \quad (38)$$

$$\begin{aligned} I'_W &= \int_0^1 dx \int_0^{1-x} dy \frac{(3 - \tan^2 \theta_W) m_W^2 + xy [(-5 + \tan^2 \theta_W) m_W^2 - \frac{1}{2}(1 - \tan^2 \theta_W) s]}{m_W^2 - y(1-y)m_Z^2 + xy(m_Z^2 - s) - i0^+} \\ &= (3 - \tan^2 \theta_W) I(\tau_W, \tau_{ZW}) + [(-5 + \tan^2 \theta_W) - 2(1 - \tan^2 \theta_W) \tau_W] J(\tau_W, \tau_{ZW}) \end{aligned} \quad (39)$$

$$\begin{aligned} I'_f &= \int_0^1 dx \int_0^{1-x} dy \frac{(4xy - 1) m_f^2}{m_f^2 - y(1-y)m_Z^2 + xy(m_Z^2 - s) - i0^+} \\ &= 4J(\tau_f, \tau_{Zf}) - I(\tau_f, \tau_{Zf}) \end{aligned} \quad (40)$$

Here, $\tau_W = s/4m_W^2$, $\tau_f = s/4m_f^2$, $\tau_{ZW} = m_Z^2/4m_W^2$, and $\tau_{Zf} = m_Z^2/4m_f^2$. I and J are given by

$$I(\tau_1, \tau_2) = \frac{1}{2} (\tau_1 - \tau_2)^{-1} (f(\tau_1) - f(\tau_2)) \quad (41)$$

$$\begin{aligned} J(\tau_1, \tau_2) &= -\frac{1}{8} (\tau_1 - \tau_2)^{-1} [1 - (\tau_1 - \tau_2)^{-1} (f(\tau_1) - f(\tau_2))] \\ &\quad + \frac{1}{4} \tau_2 (\tau_1 - \tau_2)^{-2} (g(\tau_1) - g(\tau_2)) \end{aligned} \quad (42)$$

with f and g defined by

$$f(\tau) = \begin{cases} [\sin^{-1} \sqrt{\tau}]^2 & \text{for } \tau \leq 1 \\ -\frac{1}{4} \left[\ln \left(\frac{1 + \sqrt{1 - \tau^{-1}}}{1 - \sqrt{1 - \tau^{-1}}} \right) - i\pi \right]^2 & \text{for } \tau > 1 \end{cases} \quad (43)$$

$$g(\tau) = \begin{cases} -1 + \sqrt{\frac{1-\tau}{\tau}} \tan^{-1} \left(\sqrt{\frac{\tau}{1-\tau}} \right) & \text{for } \tau \leq 1 \\ -1 + \frac{1}{2} \sqrt{1 - \tau^{-1}} \ln \left(\frac{1 + \sqrt{1 - \tau^{-1}}}{1 - \sqrt{1 - \tau^{-1}}} \right) + \frac{1}{2} i\pi \sqrt{1 - \tau^{-1}} & \text{for } \tau > 1 \end{cases} \quad (44)$$

$$\sigma v_\chi = \frac{1}{32\pi} \left(1 - \frac{m_Z^2}{s} \right)^{\frac{1}{2}} \frac{\rho^2 v^2}{s} \frac{(s - m_Z^2)^2}{(s - m_H^2)^2 + m_H^2 \Gamma_H^2} |\mathcal{A}_{\gamma Z}(s)|^2 \quad (45)$$

(5) $\chi\chi \rightarrow \gamma\gamma$

$$\sum_{\text{spin}} |\mathcal{M}|^2 = \frac{\rho^2 v^2}{2} \frac{s^2}{(s - m_H^2)^2 + m_H^2 \Gamma_H^2} |\mathcal{A}_{\gamma\gamma}(s)|^2 \quad (46)$$

$$\mathcal{A}_{\gamma\gamma}(s) = \frac{ge^2}{16\pi^2 m_W} \left(I_W + \sum_f Q_f^2 N_C^f I_f \right) \quad (47)$$

$$I_W = 2 + 3\tau_W^{-1} + 3\tau_W^{-1} (2 - \tau_W^{-1}) f(\tau_W) \quad (48)$$

$$I_f = -2\tau_f^{-1} [1 + (1 - \tau_f^{-1}) f(\tau_f)] \quad (49)$$

with f defined in Eq.(43).

$$\sigma v_\chi = \frac{1}{64\pi} \rho^2 v^2 \frac{s}{(s - m_H^2)^2 + m_H^2 \Gamma_H^2} |\mathcal{A}_{\gamma\gamma}(s)|^2 \quad (50)$$

(6) $\chi\chi \rightarrow gg$

$$\sum_{\text{spin}} |\mathcal{M}|^2 = \frac{(N_C^2 - 1)}{4} \frac{\rho^2 v^2}{2} \frac{s^2}{(s - m_H^2)^2 + m_H^2 \Gamma_H^2} |\mathcal{A}_{gg}(s)|^2 \quad (51)$$

$$\mathcal{A}_{gg}(s) = \frac{gg_s^2}{16\pi^2 m_W} \sum_q I_q \quad (52)$$

where I_q is given by Eq.(49).

$$\sigma v_\chi = \frac{1}{64\pi} \frac{(N_C^2 - 1)}{4} \rho^2 v^2 \frac{s}{(s - m_H^2)^2 + m_H^2 \Gamma_H^2} |\mathcal{A}_{gg}(s)|^2 \quad (53)$$

2. Muon Anomalous Magnetic Dipole Moment

Following a similar procedure as in the QED case [37], one can readily obtain the following result for the muon anomalous magnetic dipole moment

$$a_\mu \equiv \frac{g_\mu - 2}{2} = -\frac{3\rho^2}{32\pi^4} \int_0^\infty d\xi \xi^3 \int_0^1 dx \frac{x^2(1-x)^2}{[H(x) + \xi^2]^4} \int_0^1 dz \log [1 + \chi(z)\xi^2] \quad (54)$$

where

$$H(x) = x^2 + (1-x)r_{H\mu}^2, \quad (55)$$

$$\chi(z) = z(1-z)r_{\mu\chi}^2, \quad (56)$$

with $r_{H\mu}^2 = m_H^2/m_\mu^2$ and $r_{\mu\chi}^2 = m_\mu^2/m_\chi^2$. Performing the ξ integral, we end up with a two-dimensional integration for a_μ

$$a_\mu = -\frac{\rho^2}{128\pi^4} \int_0^1 dx \int_0^1 dz \frac{N(x,z)}{D(x,z)} \quad (57)$$

where

$$N(x, z) = x^2(1-x)^2 \left[\frac{2(1-H(x)\chi(z))}{H^2(x)\chi^2(z)} - \left(1 - \frac{3}{H(x)\chi(z)}\right) \log(H(x)\chi(z)) \right] \quad (58)$$

and

$$D(x, z) = H^2(x) \left(\frac{1}{H(x)\chi(z)} - 1 \right)^3. \quad (59)$$

ACKNOWLEDGMENTS

This work was supported in parts by the National Science Council of Taiwan under Grant Nos. 99-2112-M-007-005-MY3 and 101-2112-M-001-005-MY3 as well as the WCU program through the KOSEF funded by the MEST (R31-2008-000-10057-0). AZ was supported by the NSF under Grant No. PHY07-57035; he is also grateful to the Institute of Physics of the Academia Sinica, Taiwan, for its warm hospitality. TCY is grateful to NCTS and KITPC for their warm hospitalities. YST was funded in part by the Welcome Programme of the Foundation for Polish Science.

-
- [1] V. Silveira and A. Zee, Phys. Lett. B **161** (1985) 136.
 - [2] J. McDonald, Phys. Rev. **D50** (1994) 3637.
 - [3] C. P. Burgess, M. Pospelov and T. ter Veldhuis, Nucl. Phys. B **619**, 709 (2001) [hep-ph/0011335].
 - [4] Y. Cai, X.-G. He and B. Ren, Phys. Rev. D **83**, 083524 (2011) [arXiv:1102.1522 [hep-ph]].
 - [5] M. Gonderinger, Y. Li, H. Patel and M. J. Ramsey-Musolf, JHEP **1001**, 053 (2010) [arXiv:0910.3167 [hep-ph]].
 - [6] H. Davoudiasl, R. Kitano, T. Li and H. Murayama, Phys. Lett. B **609**, 117 (2005) [hep-ph/0405097].
 - [7] A. Drozd, B. Grzadkowski and J. Wudka, JHEP **1204**, 006 (2012) [arXiv:1112.2582 [hep-ph]].
 - [8] E. Komatsu *et al.* [WMAP Collaboration], Astrophys. J. Suppl. **192**, 18 (2011) [arXiv:1001.4538 [astro-ph.CO]].
 - [9] E. Aprile *et al.* [XENON100 Collaboration], arXiv:1207.5988 [astro-ph.CO].
 - [10] M. Ackermann *et al.* [The Fermi-LAT Collaboration], Phys. Rev. Lett. **107**, 241302 (2011) [arXiv:1108.3546 [astro-ph.HE]].

- [11] A. Geringer-Sameth and S. M. Koushiappas, Phys. Rev. Lett. **107**, 241303 (2011).
- [12] G. Aad *et al.* [The ATLAS Collaboration], arXiv:1207.7214 [hep-ex].
- [13] S. Chatrchyan *et al.* [The CMS Collaboration], arXiv:1207.7235 [hep-ex].
- [14] K. Cheung, P. -Y. Tseng, Y. -L. S. Tsai and T. -C. Yuan, JCAP **1205**, 001 (2012) [arXiv:1201.3402 [hep-ph]].
- [15] H. -B. Jin, S. Miao and Y. -F. Zhou, arXiv:1207.4408 [hep-ph].
- [16] R. Porto and A. Zee, Phys. Lett. **B666**, 491, 2008 [arXiv:0712.0448v3 [hep-ph]]; Phys. Rev. D **79**, 013003, 2009 [arXiv: 0807.0612 [hep-ph]]; Y. BenTov and A. Zee, arXiv: 1207.0467 [hep-ph].
- [17] B. W. Lee, C. Quigg and H. B. Thacker, Phys. Rev. D **16**, 1519 (1977).
- [18] D. N. Spergel and P. J. Steinhardt, Phys. Rev. Lett. **84**, 3760 (2000) [astro-ph/9909386].
- [19] D. E. Holz and A. Zee, Phys. Lett. **B517**, 239-242 (2001) [hep-ph/0105284].
- [20] A. Djouadi, A. Falkowski, Y. Mambrini and J. Quevillon, arXiv:1205.3169 [hep-ph]; A. Djouadi, O. Lebedev, Y. Mambrini and J. Quevillon, Phys. Lett. B **709**, 65 (2012) [arXiv:1112.3299 [hep-ph]].
- [21] G. Belanger, F. Boudjema, P. Brun, A. Pukhov, S. Rosier-Lees, P. Salati and A. Semenov, Comput. Phys. Commun. **182**, 842 (2011) [arXiv:1004.1092 [hep-ph]].
- [22] A. Goudelis, Y. Mambrini and C. Yaguna, JCAP **0912** (2009) 008 [arXiv:0909.2799 [hep-ph]].
- [23] C. E. Yaguna, JCAP **0903**, 003 (2009) [arXiv:0810.4267 [hep-ph]].
- [24] M. Ackermann *et al.* [LAT Collaboration], arXiv:1205.2739 [astro-ph.HE].
- [25] L. Roszkowski, E. M. Sessolo and Y. -L. S. Tsai, arXiv:1202.1503 [hep-ph].
- [26] P. Gondolo, J. Edsjo, P. Ullio, L. Bergstrom, M. Schelke and E. A. Baltz, JCAP **0407**, 008 (2004) [arXiv:astro-ph/0406204].
- [27] F. Feroz, M. P. Hobson and M. Bridges, Mon. Not. Roy. Astron. Soc. **398**, 1601 (2009) [arXiv:0809.3437 [astro-ph]].
- [28] F. Feroz and M. P. Hobson, Mon. Not. Roy. Astron. Soc. **384**, 449 (2008) [arXiv:0704.3704 [astro-ph]].
- [29] X. -G. He, S. -Y. Ho, J. Tandean and H. -C. Tsai, Phys. Rev. D **82**, 035016 (2010) [arXiv:1004.3464 [hep-ph]].
- [30] G. Aad *et al.* [ATLAS Collaboration], Phys. Lett. B **705**, 294 (2011) [arXiv:1106.5327 [Hep-ex]].

- [31] S. A. Malik, arXiv:1110.1609 [hep-ex].
- [32] Particle Data Group, Review of Particle Physics, Journal of Physics G, Nuclear and Particle Physics, Vol. **37**, No 7A 075021 (2010) and 2011 partial update for 2012 edition.
- [33] C. Weniger, arXiv:1204.2797 [hep-ph].
- [34] S. Profumo and T. Linden, arXiv:1204.6047 [astro-ph.HE].
- [35] M. Su, T. R. Slatyer and D. P. Finkbeiner, *Astrophys. J.* **724**, 1044 (2010) [arXiv:1005.5480 [astro-ph.HE]].
- [36] A. Belyaev, N. D. Christensen and A. Pukhov, arXiv:1207.6082 [hep-ph].
- [37] S. Weinberg, *The Quantum Theory of Fields, Volume I*, Cambridge University Press (1995).